

Optimization of Dark-Field CT for Lung Imaging

Peiyuan Guo^{1,2}, Simon Spindler³, Li Zhang^{1,2}, Zhentian Wang^{1,2}

¹Department of Engineering Physics, Tsinghua University, China

² Key Laboratory of Particle & Radiation Imaging (Tsinghua University) of Ministry of Education, Beijing, China

³ Institute for Biomedical Engineering, ETH Zürich and University of Zürich, Zürich, Switzerland

Abstract

Background: X-ray grating-based dark-field imaging can sense the small angle scattering caused by an object's micro-structure. This technique is sensitive to lung's porous alveoli and is able to detect lung disease at an early stage. Up to now, a human-scale dark-field CT has been built for lung imaging.

Purpose: This study aimed to develop a more thorough optimization method for dark-field lung CT and summarize principles for system design.

Methods: We proposed a metric in the form of contrast-to-noise ratio (CNR) for system parameter optimization, and designed a phantom with concentric circle shape to fit the task of lung disease detection. Finally, we developed the calculation method of the CNR metric, and analyzed the relation between CNR and system parameters.

Results: We showed that with other parameters held constant, the CNR first increases and then decreases with the system auto-correlation length (ACL). The optimal ACL is nearly not influenced by system's visibility, and is only related to phantom's property, i.e., scattering material's size and phantom's absorption. For our phantom, the optimal ACL is about 0.21 μm . As for system geometry, larger source-detector and isocenter-detector distance can increase the system's maximal ACL, helping the system meet the optimal ACL more easily.

Conclusions: This study proposed a more reasonable metric and a task-based process for optimization, and demonstrated that the system optimal ACL is only related to the phantom's property.

1 Introduction

Chronic obstructive pulmonary diseases (COPD) are a common cause of death worldwide^{1,2}. Conventional attenuation-based X-ray imaging is not suitable for detecting these diseases because X-ray is weakly absorbed by lung tissue and is not sensitive to pulmonary pathological changes. To solve this problem, X-ray grating-based dark-field imaging is a promising method. It utilizes the X-ray's wave character^{3–6} and measures dark-field signal caused by small angle scattering of an object. Since the alveoli have strong scattering properties^{7,8}, dark-field imaging can identify pathological changes of alveoli, and can be used for early detection of lung diseases.

The feasibility of dark-field imaging for lung disease detection has been widely studied, including emphysema^{9–11}, fibrosis^{12,13}, lung cancer^{14,15}, and pneumothorax¹⁶. Up to now, a dark-field chest radiography system has been built⁹ and used for patient studies¹⁷. Furthermore, a dark-field lung CT prototype has been developed by TUM¹⁸ which reaches human scale, promoting the clinical translation of dark-field CT.

As for TUM's prototype, it utilized the inverse geometry^{19,20} which means the distance between G1 and G2 is much larger than that between G0 and G1 to contain a large field of view (FOV). Besides, the gratings' lamella was perpendicular to the fan beam angle plane for fringe scanning signal retrieval method²¹. These design principles are in line with the characteristics of lung CT, so they cannot be easily changed in other designs of dark-field lung CT. For other parameters, i.e., gratings' period and their position in the CT system, quantitative optimization should be performed to determine these elements for the best performance of the system. In TUM's design, the visibility was chosen as the metric to assess system performance, which means at every point in the parameter space consisting of all the grating parameters, the visibility was calculated through wave-optical simulation, and the grating parameters with maximal visibility were selected.

This optimization method makes sense because the dark-field noise is negatively correlated to visibility²², so maximizing the visibility helps reduce noise. However, since the purpose of this system is lung imaging, and visibility is not a task-based metric, searching for the maximal visibility doesn't necessarily perform the best in lung disease detection. For a more thorough optimization process, our study proposed a new metric aiming at lung disease detection, analyzed the principles in optimization, and used them to guide our system design.

2 Methods

2.1 Dark-field imaging and CT

In a grating interferometer, fringe patterns appear at the detector plane, which is caused by a beam splitter grating noted as G1 based on either Talbot effect^{6,23} or geometrical projection²⁴. These effects require high spatial coherence, so a source grating noted as G0 can be optionally placed right after the source and split the source into multiple line sources⁴. Since in most cases the fringe period is much smaller than detector pixel size, an analyzer grating noted as G2 is introduced right before the detector to resolve the fringes. It's an absorption grating whose period is the same as the fringes and lamella is parallel to the fringes. The relation between the three gratings' period and position is shown in ⁴. To retrieve the signal contained in the fringe, the G2 translates perpendicular to the fringe pattern, and at each position it absorbs different part of the fringe, which leads to different intensity acquired by the detector, forming a phase stepping curve as:

$I_k = I_0 \cdot (1 + v \cdot \cos(\frac{2\pi k}{N} + \phi))$, where I_k means the intensity measured at the k^{th} step among the total N steps, I_0 means the mean intensity, ϕ means the phase position, and v means the visibility of the curve.

To retrieve the signals from the phase stepping curve, Fourier analysis⁶ can be used.

The retrieval of intensity can be expressed as: $I_0 = \frac{1}{N} \sum_{k=1}^N I_k$. The retrieval of visibility

can be expressed as: $v = 2 \cdot \frac{\sqrt{S_1^2 + S_2^2}}{\sum_{k=1}^N I_k}$, where $S_1 = \frac{1}{N} \sum_{k=1}^N I_k \sin(-\frac{2\pi k}{N})$, and $S_2 =$

$$\frac{1}{N} \sum_{k=1}^N I_k \cos\left(-\frac{2\pi k}{N}\right).$$

When a sample is placed in the ray path, it interacts with the incoming X-ray and cause signal change of the phase stepping curve. Apart from the conventional attenuation, if the sample is porous like lung alveoli, it will scatter the incoming ray strongly and cause visibility reduction, expressed as: $DF = -\log \frac{v_s}{v_b}$, where v_s and v_b mean the visibility measured with and without the object in the beam path. Since the dark-field signal also follows Beer-Lambert Law^{25,26} like attenuation signal, it can also be used in CT and current reconstruction methods can be applied on it.

For the quantitative description of dark-field signal, a certain material's dark-field signal of unit thickness can be calculated as $\epsilon = \sigma(G(\xi) - 1)$, where the σ is the scattering cross section, G represents the auto-correlation function which is related to the micro-structure of the material, and ξ is the auto-correlation length (ACL) representing the system's sensitivity to scattering^{27,28}, which is defined as: $\xi = \lambda \cdot \frac{L_s}{p_2}$, where λ is the wave length, p_2 is G2's period, and L_s is the distance between the object and G2 when the object is placed between G1 and G2.

2.2 Our proposed metric for optimization

In a CT image, the signal of normal lung tissue and lesions belong to two different distributions. These two distributions are overlapped, so a threshold is needed to be set to separate them. The detectability index is a metric that quantifies the separation, and for an ideal observer, it can be expressed as^{29,30}: $d'^2 = K^2 \int \frac{|F(\nu)|^2 M(\nu)^2}{N(\nu)} d\nu$, where K is the large-area transfer ratio, F is the spatial frequency spectrum of the difference between the signal and background, M is the system modulation transfer function, and N is the noise power spectrum.

Since the standard form of detectability index is hard to calculate, here we use the

$$\text{simplified form that assumes the two distributions are Gaussian}^{31}: d' = \frac{~~_2 - ~~_1}{\sqrt{\frac{1}{2}\sigma_1^2 + \frac{1}{2}\sigma_2^2}},~~~~$$

where $< S >_1$ and σ_1 denotes the mean value and standard deviation of class 1 and the same for subscript 2 and class 2. Specifically, the class 1 and 2 represent the normal tissue and lesions in our study, respectively. The simplified detectability index has a form similar to contrast-to-noise ratio (CNR), which is to be used as the metric in our following optimization.

2.3 Our phantom for optimization

To evaluate the CNR performance of different parameter point, we propose a concentric circle phantom, as shown in Figure 1. The outer ring of the phantom is filled with normal alveoli, and the inner ring is filled with emphysematous alveoli, which is a common result of COPD². The diameter of this phantom is set to 300 mm, representing human's average lung dimension³². The CNR is calculated between the two parts of this phantom according to subsection 2.2.

However, the dark-field signal of alveoli at different stage is hard to measure, so we use PMMA micro spheres to mimic alveoli's dark-field signal. According to previous studies³³, micro spheres with a diameter of 200 um has a dark-field similar to normal alveoli's, which can be used in the phantom. For emphysema, its dark-field signal is lower, so it can be replaced with 400-um-diameter spheres. The dark-field of these spheres at different ACL has been measured in³³, which can be used to calculate the phantom's dark-field signal given different ACLs.

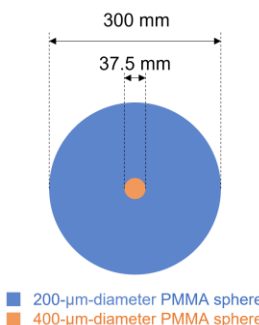


Figure 1 The concentric-circle shaped phantom simulating the task of lung disease detection.

2.3 Calculation process of CNR

To calculate the phantom's CNR, the signal flow of dark-field should be analyzed, which consists of the following steps:

- (a) The generation of dark-field signal: For each voxel, its dark-field signal, or called as linear diffusion coefficient³⁴, is determined by the system ACL as mentioned in subsection 2.1.
- (b) In the acquisition process of CT, the linear diffusion coefficient integrates along the ray path, and the total dark-field signal in projection domain leads to the visibility reduction of the fringes on the detector, which can be expressed as $DF = \int \epsilon dx = \mathcal{R}(\epsilon)$.
- (c) Due to the quantum noise of the raw data acquired by the detector, the retrieved visibility is also corrupted with noise through phase-stepping and signal retrieval. Therefore, the dark-field noise can be expressed as $\sigma_{DF}^2 = \frac{1}{NI_0v^2}(\nu^2(1 + \exp(T)) + 2(1 + \exp(T + 2DF)))$ based on the analysis in ²², where the T means the attenuation signal following $T = \mathcal{R}(\mu)$ where μ is the linear attenuation coefficient. The visibility can be calculated through wave-optical simulation³⁵. The expression can be further written as $\sigma_{DF}^2 = \frac{1}{NI_0v^2}Noise(DF, T, \nu)$
- (d) In the reconstruction process, the noise propagates from projection domain into the reconstruction voxels, which can be expressed as $\sigma_\epsilon^2 = \mathcal{R}^{-1^2}(\sigma_{DF}^2)$. Since the reconstruction is a linear process, the noise propagation can also be calculated analytically, as studied in ³⁶.

Combining the analysis above, the dark-field CNR of the phantom can be calculated as:

$$CNR = \frac{1}{\sqrt{NI_0}\cdot\nu} \cdot \frac{\epsilon_1(\xi) - \epsilon_2(\xi)}{|\mathcal{R}^{-1^2}(Noise(\mathcal{R}(\epsilon(\xi)), \mathcal{R}(\mu), \nu))|}.$$

3 Results

3.1 Optimal ACL for CNR

According to the former analysis, the phantom's CNR can be treated as a function of ACL, visibility, and phantom's property including size and absorption. If the visibility and phantom are fixed, as the ACL increases, the CNR first increases and then decreases as shown in Figure 2. This can be explained by that when ACL is small, increasing ACL leads to increasing dark-field signal, causing the CNR goes up, and after a turning point, the dark-field noise increases more significantly than the signal itself, leading to a decrease of CNR. The turning point is the optimal ACL where the CNR is the highest with a given visibility and phantom.

Here we set the visibility to 0.2 and use our proposed phantom, and calculate the CNR at different ACL. Since the CNR is related to the intensity, the CNR in this curve is in arbitrary unit. However, the shape of this curve proves the existence of optimal ACL.

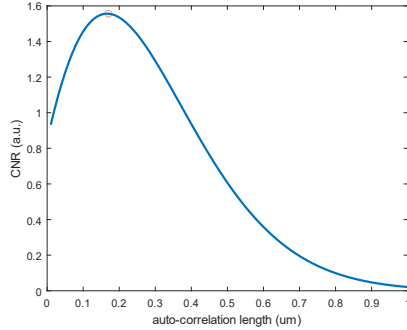


Figure 2 The CNR at different ACL with given phantom and visibility.

3.2 Optimal ACL with visibility

The relationship between CNR and optimal ACL with visibility is studied here. The visibility was set from 0.1 to 0.4, covering the common range in grating interferometer. It can be observed in Figure 3 that, although the visibility definitely influences the CNR value through noise, it has almost no impact on the optimal ACL. The fluctuation of optimal ACL within this visibility range is less than 2%, which can be neglected in the following analysis.

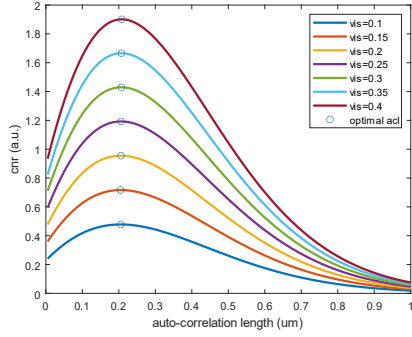


Figure 3 The CNR at different ACL with different visibility.

3.3 Optimal ACL with phantom

The impact of phantom's property on optimal ACL is also studied. In this part, the visibility is set to 0.2. First, the diameter of the phantom varies from 150 mm to 300 mm, and through calculation it can be observed that the optimal ACL decreases as the diameter increases. Second, the transmission factor of the phantom varies from half of to twice the original value, and the optimal ACL decreases as the transmission value increases. Besides, the change of optimal ACL at different transmission level is rather small, which means the optimal ACL is more sensitive to phantom's dark-field level than transmission.

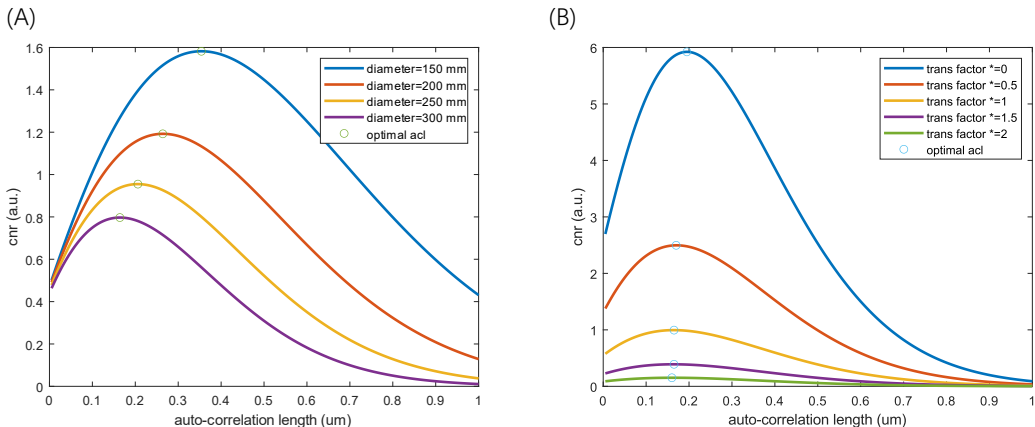


Figure 4 The CNR at different ACL with different phantom (A) diameter and (B) attenuation.

3.4 Influence of system geometry

Before designing the system, the visibility of different parameter point is calculated through wave optical simulation. It can be observed that the visibility fluctuates

unobviously among the parameter space with the same grating structural height, which can be attributed to limits on grating periods and positions caused by the large bore size between G1 and G2. Combining this finding with the constant optimal ACL, it can be found that the system has its highest CNR as long as it reaches the optimal ACL. However, the G2 period has a lower limit due to the limits on G0 and G1's period and position, causing an upper limit on system's ACL. Therefore, the key point in designing such a system is to reach the optimal ACL.

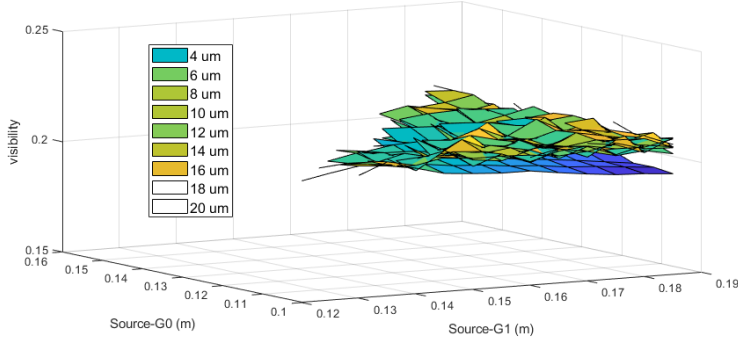


Figure 5 The simulated visibility at different parameter point.

System geometry, like source-detector and isocenter-detector distance, determines the forward-projection and reconstruction process, which may influence the optimal ACL. Through simulation, we found the optimal ACL does not change at different system geometries. However, increased source-detector and isocenter-detector distance can increase the upper bound of ACL, making the system meet the optimal ACL more easily.

3.5 A design for dark-field lung CT

We calculated the CNR at each parameter point within the parameter space adapted from TUM's design¹⁸, and plotted it with corresponding ACL as shown in Figure 6. It can be observed that the curve's shape was similar to Figure 2, and its vibration can be attributed to the slight change of visibility. Its optimal ACL was about 0.21 um at the design energy of 60 keV, which was slightly larger than system's maximum ACL limited by current system geometry. However, if the rotation center can be moved closer to G2, the maximum ACL becomes larger and the optimal ACL can be easily reached because the distance between G0 and G1 increases. Besides, the periods of G0 and G1

are larger than current geometry, as shown in Table 1. Furthermore, if the system total length (distance between source and G2) can slightly increase from 1050 mm to 1100 mm, the period of G0 and G1 can even increase over 25% at the same ACL, which benefits grating fabrication and can improve system performance.

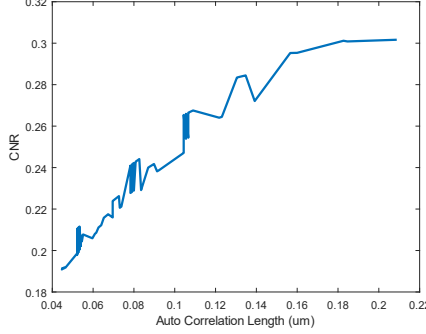


Figure 6 The CNR with ACL at different parameter point.

Table 1 For current (adapted from ¹⁸), loose (isocenter closer to G2), and extended (increased source-G2 distance) geometry, the grating position, period and ACL at best system performance.

Geometry	Current	Loose	Extended
Source-G0 (mm)	100	100	100
Source-G1 (mm)	187	250	300
Source-G2 (mm)	1050	1050	1100
Source-isocenter (mm)	570	650	700
p_0 (um)	5.28	7.5	10
p_1 (um)	4.8	6.3	8
p_2 (um)	52.41	40	40
ACL (um)	0.19	0.21	0.21

4 Discussion

Based on the simulation in section 3, we found that the grating-based CT system has an optimal ACL for highest dark-field CNR, and it's only related to the phantom's property. This can lead to three findings: First, no matter what type of grating interferometer is used (i.e., Talbot-Lau, geometrical projection, dual-phase³⁷...), its optimal ACL

remains unchanged given the same phantom. Second, in simulation grating imperfections and bridges²⁰ can be taken into consideration to calculate visibility more accurately. Here we show that these considerations can obtain a more precise CNR, but the optimal ACL is the same regardless of the consideration. Third, since the optimal ACL is related to phantom's size and absorption, if the phantom is changed, i.e., the dark-field CT is designed for other purpose like security inspection, the optimal ACL will be different.

We have to point that the current phantom design is rather naïve. A potential improvement of this study is to design a more realistic phantom similar to human chest shape. Besides, although the current phantom's absorption may be slightly lower than a real human chest due to absence of rib cage and spine, the circle shape and the diameter of the phantom make it scatters stronger than real human lungs. Since dark-field strength has more influence on optimal ACL than attenuation as shown in subsection 3.3, the optimal ACL may be higher for real human body than this phantom.

Although we have found the existence of optimal ACL, we have to point out the possibility that a lower ACL than the optimal one may lead to higher CNR due to grating fabrication issues. For example, when the system ACL is smaller than the optimal, the grating period can be larger based on aforementioned equation. For a larger period, the grating can achieve a higher structural height, or less grating imperfection and bridge fraction at the same structural height, which leads to a higher visibility³⁸. Since the CNR is positively related to visibility, the CNR can be even higher than that of optimal ACL. However, the quantitative description of grating fabrication quality with grating period and structural height has not been thoroughly studied, but we can empirically recommend an ACL lower than the optimal one especially when the absorption gratings' period is low.

5 Conclusion

In this study, we proposed a metric in the form of CNR for dark-field CT optimization, and designed a concentric circle shape phantom representing the task of lung disease detection. We found that the system has an optimal ACL, which is only related to phantom's property, and is nearly irrelevant with visibility. We hope our work can make the system optimization more precise, and provide intuitive principles on system design.

Reference

1. Quaderi SA, Hurst JR. The unmet global burden of COPD. *Global Health, Epidemiology and Genomics*. 2018;3:e4. doi:10.1017/gheg.2018.1
2. Sullivan J, Pravosud V, Mannino DM, Siegel K, Choate R, Sullivan T. National and State Estimates of COPD Morbidity and Mortality — United States, 2014-2015. *Chronic Obstr Pulm Dis*. 5(4):324-333. doi:10.15326/jcopdf.5.4.2018.0157
3. Weitkamp T, Diaz A, David C, et al. X-ray phase imaging with a grating interferometer. *Opt Express, OE*. 2005;13(16):6296-6304. doi:10.1364/OPEX.13.006296
4. Weitkamp T, David C, Kottler C, Bunk O, Pfeiffer F. Tomography with grating interferometers at low-brilliance sources. In: *Developments in X-Ray Tomography V*. Vol 6318. SPIE; 2006:249-258. doi:10.1117/12.683851
5. Momose A, Takeda T, Itai Y, Hirano K. Phase-contrast X-ray computed tomography for observing biological soft tissues. *Nat Med*. 1996;2(4):473-475. doi:10.1038/nm0496-473
6. Pfeiffer F, Bech M, Bunk O, et al. X-ray dark-field and phase-contrast imaging using a grating interferometer. *Journal of Applied Physics*. 2009;105(10):102006. doi:10.1063/1.3115639
7. Urban T, Sauter AP, Frank M, et al. Dark-Field Chest Radiography Outperforms Conventional Chest Radiography for the Diagnosis and Staging of Pulmonary Emphysema. *Invest Radiol*. 2023;58(11):775-781. doi:10.1097/RLI.0000000000000989
8. Willer K, Fingerle AA, Gromann LB, et al. X-ray dark-field imaging of the human lung—A feasibility study on a deceased body. *PLOS ONE*. 2018;13(9):e0204565. doi:10.1371/journal.pone.0204565
9. Willer K, Fingerle AA, Noichl W, et al. X-ray dark-field chest imaging for detection and quantification of emphysema in patients with chronic obstructive pulmonary

disease: a diagnostic accuracy study. *The Lancet Digital Health*. 2021;3(11):e733-e744. doi:10.1016/S2589-7500(21)00146-1

10. Urban T, Gassert FT, Frank M, et al. Qualitative and Quantitative Assessment of Emphysema Using Dark-Field Chest Radiography. *Radiology*. 2022;303(1):119-127. doi:10.1148/radiol.212025
11. Meinel FG, Yaroshenko A, Hellbach K, et al. Improved Diagnosis of Pulmonary Emphysema Using In Vivo Dark-Field Radiography. *Investigative Radiology*. 2014;49(10):653. doi:10.1097/RLI.0000000000000067
12. Gassert FT, Urban T, Pfeiffer D, Pfeiffer F. Dark-Field Chest Radiography of Combined Pulmonary Fibrosis and Emphysema. *Radiology: Cardiothoracic Imaging*. 2022;4(4):e220085. doi:10.1148/ryct.220085
13. Nelson BJ, Leng S, Koenig T, McCollough CH. Complementary use of x-ray dark-field and attenuation computed tomography in quantifying pulmonary fibrosis in a mouse model. In: *Medical Imaging 2022: Biomedical Applications in Molecular, Structural, and Functional Imaging*. Vol 12036. SPIE; 2022:253-263. doi:10.1117/12.2612877
14. Scherer K, Yaroshenko A, Bölkbas DA, et al. X-ray Dark-field Radiography - In-Vivo Diagnosis of Lung Cancer in Mice. *Sci Rep*. 2017;7(1):402. doi:10.1038/s41598-017-00489-x
15. Guo P, Zhang L, Lu J, et al. Grating-based x-ray dark-field CT for lung cancer diagnosis in mice. *European Radiology Experimental*. 2024;8(1):12. doi:10.1186/s41747-023-00399-w
16. Hellbach K, Baehr A, De Marco F, et al. Depiction of pneumothoraces in a large animal model using x-ray dark-field radiography. *Sci Rep*. 2018;8(1):2602. doi:10.1038/s41598-018-20985-y
17. Kattau M, Willer K, Noichl W, et al. X-ray dark-field chest radiography: a reader study to evaluate the diagnostic quality of attenuation chest X-rays from a dual-contrast scanning prototype. *Eur Radiol*. Published online February 18, 2023. doi:10.1007/s00330-023-09477-4
18. Viermetz M, Gustschin N, Schmid C, et al. Dark-field computed tomography reaches the human scale. *PNAS*. 2022;119(8). doi:10.1073/pnas.2118799119
19. Donath T, Chabior M, Pfeiffer F, et al. Inverse geometry for grating-based x-ray phase-contrast imaging. *Journal of Applied Physics*. 2009;106(5):054703. doi:10.1063/1.3208052
20. Viermetz M, Gustschin N, Schmid C, et al. Technical Design Considerations of a Human-Scale Talbot-Lau Interferometer for Dark-Field CT. *IEEE Transactions on*

Medical Imaging. 2023;42(1):220-232. doi:10.1109/TMI.2022.3207579

21. Kottler C, Pfeiffer F, Bunk O, Grünzweig C, David C. Grating interferometer based scanning setup for hard x-ray phase contrast imaging. *Review of Scientific Instruments.* 2007;78(4):043710. doi:10.1063/1.2723064
22. Revol V, Kottler C, Kaufmann R, Straumann U, Urban C. Noise analysis of grating-based x-ray differential phase contrast imaging. *Review of Scientific Instruments.* 2010;81(7):073709. doi:10.1063/1.3465334
23. Momose A, Kawamoto S, Koyama I, Hamaishi Y, Takai K, Suzuki Y. Demonstration of X-Ray Talbot Interferometry. *Jpn J Appl Phys.* 2003;42(7B):L866. doi:10.1143/JJAP.42.L866
24. Huang ZF, Kang KJ, Zhang L, et al. Alternative method for differential phase-contrast imaging with weakly coherent hard x rays. *Phys Rev A.* 2009;79(1):013815. doi:10.1103/PhysRevA.79.013815
25. Yashiro W, Terui Y, Kawabata K, Momose A. On the origin of visibility contrast in x-ray Talbot interferometry. *Opt Express, OE.* 2010;18(16):16890-16901. doi:10.1364/OE.18.016890
26. Wang ZT, Kang KJ, Huang ZF, Chen ZQ. Quantitative grating-based x-ray dark-field computed tomography. *Appl Phys Lett.* 2009;95(9):094105. doi:10.1063/1.3213557
27. Strobl M. General solution for quantitative dark-field contrast imaging with grating interferometers. *Sci Rep.* 2014;4(1):7243. doi:10.1038/srep07243
28. Prade F, Yaroshenko A, Herzen J, Pfeiffer F. Short-range order in mesoscale systems probed by X-ray grating interferometry. *EPL.* 2015;112(6):68002. doi:10.1209/0295-5075/112/68002
29. Sharp P, Barber DC, Brown DG, et al. Report 54. *Journal of the ICRU.* 1996;os28(1):NP-NP. doi:10.1093/jicru/os28.1.Report54
30. Samei E, Bakalyar D, Boedeker KL, et al. Performance evaluation of computed tomography systems: Summary of AAPM Task Group 233. *Medical Physics.* 2019;46(11):e735-e756. doi:10.1002/mp.13763
31. Barrett HH, Myers KJ. *Foundations of Image Science.* John Wiley & Sons; 2013.
32. Bellemare F, Jeanneret A, Couture J. Sex Differences in Thoracic Dimensions and Configuration. *Am J Respir Crit Care Med.* 2003;168(3):305-312. doi:10.1164/rccm.200208-876OC
33. Spindler S, Etter D, Rawlik M, et al. The choice of an autocorrelation length in

dark-field lung imaging. *Sci Rep.* 2023;13(1):1-11. doi:10.1038/s41598-023-29762-y

34. Taphorn K, De Marco F, Andrejewski J, Sellerer T, Pfeiffer F, Herzen J. Grating-based spectral X-ray dark-field imaging for correlation with structural size measures. *Sci Rep.* 2020;10(1):13195. doi:10.1038/s41598-020-70011-3
35. Zhang R, Zhang L, Chen Z, Peng W, Li R. Sensitivity of a non-interferometric grating-based x-ray imaging system. *Phys Med Biol.* 2014;59(7):1573. doi:10.1088/0031-9155/59/7/1573
36. Wang J, Lu H, Li T, Liang Z. An alternative solution to the nonuniform noise propagation problem in fan-beam FBP image reconstruction. *Medical Physics.* 2005;32(11):3389-3394. doi:10.1118/1.2064807
37. Kagias M, Wang Z, Jefimovs K, Stampaconi M. Dual phase grating interferometer for tunable dark-field sensitivity. *Applied Physics Letters.* 2017;110(1):014105. doi:10.1063/1.4973520
38. Shi Z, Jefimovs K, Romano L, Stampaconi M. Towards the Fabrication of High-Aspect-Ratio Silicon Gratings by Deep Reactive Ion Etching. *Micromachines.* 2020;11(9):864. doi:10.3390/mi11090864